Anisotropic physical properties of the $Al_{13}Fe_4$ complex intermetallic and its ternary derivative $Al_{13}(Fe,Ni)_4$

P. Popčević,[1] A. Smontara,[1] J. Ivkov,[1] M. Wencka,[2] M. Komelj,[2] P. Jeglič,[2] S. Vrtnik,[2] M. Bobnar,[2] Z. Jagličić,[3] B. Bauer,[4] P. Gille,[4] H. Borrmann,[5] U. Burkhardt,[5] Yu. Grin,[5] and J. Dolinšek[2,*]

[1]*Institute of Physics, Laboratory for the Study of Transport Problems, Bijenička 46, P.O. Box 304, HR-10001 Zagreb, Croatia*

[2]*J. Stefan Institute, University of Ljubljana, Jamova 39, SI-1000 Ljubljana, Slovenia*

[3]*Institute of Mathematics, Physics and Mechanics, University of Ljubljana, Jadranska 19, SI-1000 Ljubljana, Slovenia*

[4]*Department of Earth and Environmental Sciences, Crystallography Section, Ludwig-Maximilians-Universität München, Theresienstrasse 41, D-80333 München, Germany*

[5]*Max-Planck-Institut für Chemische Physik fester Stoffe, Nöthnitzer Str. 40, D-01187 Dresden, Germany*

(Received 3 November 2009; revised manuscript received 16 April 2010; published 7 May 2010)

We have investigated the magnetic susceptibility, the electrical resistivity, the specific heat, the thermoelectric power, the Hall coefficient, and the thermal conductivity of the $Al_{13}Fe_4$ and $Al_{13}(Fe,Ni)_4$ monoclinic approximants to the decagonal quasicrystal. While the $Al_{13}Fe_4$ crystals are structurally well ordered, the ternary derivative $Al_{13}(Fe,Ni)_4$ contains substitutional disorder and is considered as a disordered version of the $Al_{13}Fe_4$. The crystallographic-direction-dependent measurements were performed along the a^*, b, and c directions of the monoclinic unit cell, where the (a^*,c) atomic planes are stacked along the b direction. The electronic transport and the magnetic properties exhibit significant anisotropy. The stacking b direction is the most conducting direction for the electricity and heat. The effect of substitutional disorder in $Al_{13}(Fe,Ni)_4$ is manifested in the large residual resistivity $\rho(T\rightarrow 0)$ and significantly reduced thermal conductivity of this compound, as compared to the ordered $Al_{13}Fe_4$. Specific-heat measurements reveal that the electronic density of states at the Fermi level of both compounds is high. The anisotropic Hall coefficient R_H reflects complex structure of the anisotropic Fermi surface that contains electronlike and holelike contributions. Depending on the combination of directions of the current and the magnetic field, electronlike ($R_H<0$) or holelike ($R_H>0$) contributions may dominate, or the two contributions compensate each other ($R_H\approx 0$). Similar complicated anisotropic behavior was observed also in the thermopower. The anisotropic Fermi surface was calculated *ab initio* using the atomic parameters of the refined $Al_{13}Fe_4$ structural model that is also presented in this work.

DOI: 10.1103/PhysRevB.81.184203 PACS number(s): 61.44.Br, 71.23.Ft

I. INTRODUCTION

One of the basic open questions in the physics of quasicrystals (QCs) is whether the quasiperiodicity of the structure influences the physical properties of a solid in a fundamental way by introducing qualitatively new phenomena or the unusual properties are rather a consequence of complex local atomic order with no direct relationship to the quasiperiodicity. In order to elucidate this question, decagonal quasicrystals (d-QCs) are of particular importance due to the fact that their structure can be viewed as a periodic stacking of quasiperiodic atomic planes, so that d-QCs are two-dimensional quasicrystals, whereas they are periodic crystals in a direction perpendicular to the quasiperiodic planes. Physical properties of the d-QCs can be consequently studied along the quasiperiodic (Q) and periodic (P) crystallographic directions on the same sample. A consequence of the structural anisotropy of d-QCs are anisotropic electrical and thermal transport properties [the electrical resistivity ρ,[1–3] the thermoelectric power S,[4] the Hall coefficient R_H,[5,6] the thermal conductivity κ,[7,8] and the optical conductivity $\sigma(\omega)$ (Ref. 9)], when measured along the Q and P directions. The electrical resistivity generally shows positive temperature coefficient (PTC) at metallic values along the P direction, whereas the resistivity in the quasiperiodic plane is considerably larger and exhibits negative temperature coefficient (NTC) and sometimes also a maximum somewhere below room temperature (RT) or a leveling-off upon $T\rightarrow 0$. The anisotropy of the Hall coefficient R_H is another intriguing feature of d-QCs, being positive holelike ($R_H>0$) for the magnetic field lying in the quasiperiodic plane, whereas it changes sign to negative ($R_H<0$) for the field along the periodic direction, thus becoming electronlike. This R_H anisotropy was reported for the d-Al-Ni-Co, d-Al-Cu-Co, and d-Al-Si-Cu-Co and is considered to be a universal feature of d-QCs.[5,6]

The degree of anisotropy of the transport coefficients is related to the structural details of a particular decagonal phase, depending on the number of quasiperiodic layers in one periodic unit.[10,11] The most anisotropic case are the phases with just two layers, realized in d-Al-Ni-Co and d-Al-Cu-Co, where the periodicity length along the periodic axis is about 0.4 nm and the resistivity ratio at RT amounts typically $\rho_Q/\rho_P\approx 6-10$.[1–3] Other d phases contain more quasiperiodic layers in a periodic unit and show smaller anisotropies. In d-Al-Co, d-Al-Ni, and d-Al-Si-Cu-Co there are four quasiperiodic layers with periodicity about 0.8 nm and the RT anisotropy is $\rho_Q/\rho_P\approx 2-4$.[4] d-Al-Mn, d-Al-Cr, and d-Al-Pd-Mn phases contain six layers with the periodicity of about 1.2 nm and the anisotropy amounts $\rho_Q/\rho_P\approx 1.2-1.4$, whereas d-Al-Pd and d-Al-Cu-Fe phases with eight layers in a periodicity length of 1.6 nm are close to

isotropic. While the origin of the anisotropic electron transport coefficients is the anisotropic Fermi surface, the anisotropy of which originates from the specific stacked-layer crystal structure of the *d*-QC phases and the chemical decoration of the lattice, the lack of translational periodicity within the quasiperiodic planes prevents any quantitative theoretical analysis of this phenomenon. The problem can be overcome by considering approximant phases to the decagonal phase, for which—being periodic solids in three dimensions—theoretical simulations are straightforward to perform. Approximant phases are characterized by large unit cells, which periodically repeat in space with the atomic decoration closely resembling that of *d*-QCs. Atomic layers are again stacked periodically and the periodicity lengths along the stacking direction are almost identical to those along the periodic direction of *d*-QCs. Moreover, atomic planes of the approximants and the *d*-QCs show locally similar patterns, so that their structures on the scale of near-neighbor atoms closely resemble each other. Decagonal approximants thus offer valid comparison to the *d*-QCs.

Recently, the anisotropic magnetic and transport properties (the magnetic susceptibility, the electrical resistivity, the thermoelectric power, the Hall coefficient, and the thermal conductivity), measured along three orthogonal crystallographic directions, were reported for three decagonal approximant phases of increasing structural complexity comprising two, four, and six atomic layers in the unit cell. The first was the $Al_{76}Co_{22}Ni_2$,[12,13] known as the Y phase of Al-Ni-Co (denoted as Y-Al-Ni-Co), which belongs to the $Al_{13}TM_4$ (*TM* =transition metal) family of complex intermetallic compounds and is a monoclinic approximant to the decagonal phase with two atomic layers within one periodic unit of ≈ 0.4 nm along the stacking direction and a relatively small unit cell, comprising 32 atoms. The second was the orthorhombic o-$Al_{13}Co_4$ decagonal approximant,[14] also belonging to the $Al_{13}TM_4$ family, but comprising four atomic layers within one periodic unit of ≈ 0.8 nm along the stacking direction and a larger unit cell comprising 102 atoms. The third was the $Al_4(Cr,Fe)$ compound with composition $Al_{80}Cr_{15}Fe_5$,[15,16] belonging to the family of orthorhombic Al_4TM phases first described by Deng *et al.*,[17] which are approximants to the decagonal phase with six atomic layers in a periodic unit of 1.25 nm and 306 atoms in the giant unit cell. Common to all these phases is strong anisotropy of the magnetic and transport properties between the stacking and the in-plane directions, where the crystals show the highest conductivity for both the electricity and heat along the stacking direction (corresponding to the periodic direction in *d*-QCs), whereas the in-plane anisotropy is considerably smaller, yet significant. For the phases Y-Al-Ni-Co and o-$Al_{13}Co_4$, the origin of the anisotropy was analyzed in terms of the *ab initio* calculated anisotropic Fermi surface, using published structural models.

In this paper we present anisotropic physical properties of two other decagonal approximant phases from the $Al_{13}TM_4$ family of complex intermetallic compounds, the monoclinic $Al_{13}Fe_4$ and its ternary substitution derivative $Al_{13}(Fe,Ni)_4$, both comprising four atomic layers within one periodic unit of ≈ 0.8 nm along the stacking direction and a unit cell comprising 102 atoms. The $Al_{13}Fe_4$ crystals can be currently grown to the highest structural perfection within the $Al_{13}TM_4$ family, containing small amount of quenched structural disorder. The introduction of a small amount of Ni atoms into the ternary extension $Al_{13}(Fe,Ni)_4$ (about 2 at. % in our case) creates disorder, so that the comparison of $Al_{13}Fe_4$ and $Al_{13}(Fe,Ni)_4$ demonstrates the effect of substitutional disorder on the physical properties of decagonal approximants and, more generally, of complex intermetallic compounds. The high structural quality of our $Al_{13}Fe_4$ samples allowed us to refine the structural model of the $Al_{13}Fe_4$ phase by an x-ray diffraction study, so that this model is another achievement of this paper.

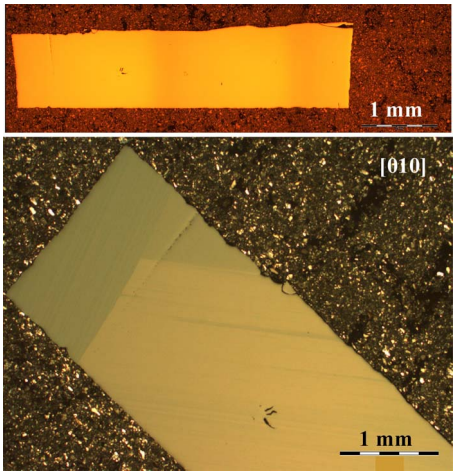

FIG. 1. (Color online) Microstructure of the $Al_{13}Fe_4$ material in bright (top) and polarized (bottom) light, visualizing formation of the twins in the (010) plane.

II. STRUCTURAL CONSIDERATIONS AND SAMPLE PREPARATION

The group of decagonal approximants with the composition $Al_{13}TM_4$ comprises monoclinic $Al_{13}Fe_4$,[18] orthorhombic o-$Al_{13}Co_4$,[19] monoclinic m-$Al_{13}Co_4$,[20] monoclinic $Al_{13-x}(Co_{1-y}Ni_y)_4$ (the Y phase),[21] monoclinic $Al_{13}Os_4$,[22] $Al_{13}Ru_4$ (isotypical to $Al_{13}Fe_4$),[23] and $Al_{13}Rh_4$ (also isotypical to $Al_{13}Fe_4$).[24] According to the $Al_{13}Fe_4$ structural model by Grin *et al.*,[18] lattice parameters of the monoclinic unit cell (space group $C2/m$, Pearson symbol $mC102$) are $a=1.5492$ nm, $b=0.8078$ nm, $c=1.2471$ nm, and $\beta=107.69°$ with 102 atoms in the unit cell. All lattice sites are fully occupied (occupancy 1) except the site Al(2) that shows partial occupation of 0.92 ± 0.02. The structure can be described as a four-layer stacking along [010],[18,21] with flat layers at $y=0$ and 1/2 and two symmetrically equivalent puckered layers at $y=1/4$ and 3/4, giving ≈ 0.8 nm periodicty along [010].

The $Al_{13}Fe_4$ and $Al_{13}(Fe,Ni)_4$ single crystals used in our study were grown by the Czochralski technique and the details of preparation are described elsewhere.[25] The samples of $Al_{13}Fe_4$ tend to form twins in the (010) plane (Fig. 1). The specimens for the physical measurements were cut from the nontwinned parts of the crystal. The $Al_{13}(Fe,Ni)_4$ phase is a ternary solid solution of Ni in $Al_{13}Fe_4$ with the maximum

TABLE I. Comparison of the $Al_{13}Fe_4$ crystallographic data for the refined model (this work) and the original model (Ref. 18).

	Refined model (this work)	Original model (Ref. 18)
a, Å	15.488(1)	15.492(2)[a]
b, Å	8.0866(5)	8.078(2)[a]
c, Å	12.4769(8)	12.471(1)[a]
β, deg	107.669(4)	107.69(1)[a]
Cell volume, Å^3	1489.0(3)	1486.9 (9)
Calculated density (g cm^{-3})	3.842	3.844
Absorption coefficient (cm^{-1})	35.67	414.53
Radiation; wavelength, Å	Ag $K\alpha$; 0.56087	Mo $K\alpha$; 0.71073
Diffractometer	Rigaku R-Axis	Siemens R3m/V
Mode of refinement	$F(hkl)$	$F(hkl)$
Cutoff	$F(hkl)>4\sigma(F)$	$F(hkl)>4\sigma(F)$
$2\theta_{max}$; $(\sin\theta/\lambda)_{max}$	122.40; 1.562	27.4; 0.7
$N(hkl)$ measured	61229	1892
$N(hkl)$ unique used for refinement	13788	1127
N parameters refined	137	137
$R(F)$	0.041	0.053

[a]The lattice parameters were obtained from Guinier x-ray powder diffraction data.

solubility of Ni 8.9 at. % (Ref. 26) and is considered as an approximant phase to the $Al_{71}Ni_{24}Fe_5$ decagonal quasicrystal.[27] The chemical composition of the $Al_{13}(Fe,Ni)_4$ single crystal used for our investigations was $Al_{76.5}Fe_{21.3}Ni_{2.2}$.

The x-ray diffraction experiment was made on a nearly isometric $Al_{13}Fe_4$ single crystal of 50 μm average size. The high quality of the crystal allowed collecting the diffraction data up to a very high-diffraction angle of $2\theta_{max}=122.4°$. In this way, a high-resolution diffraction data set was obtained, enabling us to refine the currently existing structural model of $Al_{13}Fe_4$.[18] In the present study, we obtained a unique data set with the extremely high ratio $N(hkl)_{\text{used for refinement}}/N_{\text{refined parameters}}$ of 104 compared with 9 in Ref. 18. In the following, the structural model presented in this work is referred to as the refined model, whereas the model of Ref. 18 is referred to as the original model. All crystallographic calculations were performed with the program package WINCSD.[28] The crystallographic information of the original and the refined models is compared in Table I, whereas the final atomic coordinates and the displacement parameters of the refined model are listed in Table II. The refined atomic coordinates are within 3 e.s.d. equal to the atomic coordinates of the original model. In the refined model, the occupancy of the position Al(15) [that corresponds to the partially occupied position Al(2) of the original model] was found to be 1 within 1 e.s.d., so that all lattice sites of the refined model are fully occupied. The slightly enhanced displacement parameters for this position are probably originating from the local environment and, eventually, from the partial local symmetry breaking. Thus, in comparison with many other members of the $Al_{13}TM_4$ family, the $Al_{13}Fe_4$ reveals a nearly completely ordered crystal structure.

In order to perform crystallographic-direction-dependent studies, we have cut from the single crystal of each compound three bar-shaped samples of dimensions $1\times1\times8$ mm^3, with their long edges along three orthogonal directions. The long edge of the first sample was along the [010] stacking direction (designated in the following as b), which corresponds to the periodic direction in the related d-QCs. The (a,c) monoclinic plane corresponds to the quasiperiodic plane in the d-QCs and the second sample was cut with the long edge along the [001] direction (designated as c), whereas the third one was cut with the long edge along the direction perpendicular to the (b,c) plane. This direction is designated as a^*, it lies in the monoclinic plane at an angle 17° with respect to [100] and perpendicular to [001]. For each sample, the orientation of the other two crystallographic directions was also known. The so-prepared samples enabled us to determine the anisotropic physical properties along the three orthogonal directions of the investigated monoclinic crystal structures of $Al_{13}Fe_4$ and $Al_{13}(Fe,Ni)_4$.

III. EXPERIMENTAL RESULTS

A. ^{27}Al NMR spectra

We first give experimental evidence that the $Al_{13}(Fe,Ni)_4$ crystal can be viewed as a structurally disordered version of the well-ordered $Al_{13}Fe_4$, using ^{27}Al NMR spectroscopy. The ^{27}Al NMR spectra of both compounds for the magnetic field oriented along the a^*, b, and c crystallographic directions are displayed superposed in Fig. 2. The spectra were recorded in a magnetic field $B=9.39$ T at the temperature 80 K by a frequency-sweep technique. We observe that for all three orientations, the spectrum of $Al_{13}Fe_4$ is a multiplet of sharp lines, whereas the spectrum of $Al_{13}(Fe,Ni)_4$ is broad and more or less featureless, extending over the entire frequency range of the $Al_{13}Fe_4$ spectrum. This broadening can be explained by the positional and substitutional disorder in the

TABLE II. Atomic coordinates and displacement parameters of the $Al_{13}Fe_4$ refined model. $B_{eq}=1/3[B_{11}a^{*2}a^2+\cdots 2B_{23}b^*c^*bc\cos(\alpha)]$. The anisotropic displacement parameters can be obtained from the authors.

Atom	Site	x	y	z	B_{eq} (Å^{-2})
Fe(1)	4(i)	0.58547(2)	0	0.38244(2)	0.338(3)
Fe(2)	4(i)	0.09808(2)	0	0.37654(2)	0.299(3)
Fe(3)	4(i)	0.40945(2)	0	0.01148(2)	0.333(3)
Fe(4)	4(i)	0.09742(2)	0	0.01426(2)	0.326(3)
Fe(5)	8(j)	0.31973(1)	0.20658(3)	0.27779(2)	0.347(2)
Al(1)	4(i)	0.56605(6)	0	0.17393(7)	0.53(1)
Al(2)	4(i)	0.42642(6)	0	0.41972(7)	0.50(1)
Al(3)	4(i)	0.25909(6)	0	0.03874(9)	0.70(1)
Al(4)	4(i)	0.02071(6)	0	0.17091(7)	0.50(1)
Al(5)	4(i)	0.26256(6)	0	0.46521(9)	0.73(1)
Al(6)	4(i)	0.41360(6)	0	0.21180(7)	0.47(1)
Al(7)	8(j)	0.68555(4)	0.21760(8)	0.11092(5)	0.518(8)
Al(8)	2(b)	0	0	1/2	0.57(2)
Al(9)	4(g)	1/2	0.2505(1)	0	0.51(1)
Al(10)	8(j)	0.67829(4)	0.22012(8)	0.33435(5)	0.555(8)
Al(11)	8(j)	0.86329(4)	0.21951(8)	0.47851(5)	0.535(8)
Al(12)	4(i)	0.19447(6)	0	0.22725(7)	0.50(1)
Al(13)	8(j)	0.86793(4)	0.21195(8)	0.10985(5)	0.527(8)
Al(14)	8(j)	0.99182(4)	0.23283(8)	0.32987(5)	0.535(8)
Al(15)	4(i)	0.82305(8)	0	0.28158(9)	0.90(2)

$Al_{13}(Fe,Ni)_4$ lattice, created by the introduction of about 2 at. % of Ni. The ^{27}Al nucleus has spin $I=5/2$ and possesses electric quadrupole moment, which couples to the electric field gradient tensor produced at the ^{27}Al site by the neighboring ionic and electronic charges. The ^{27}Al resonance frequency is thus sensitively determined by the charge distribution within the local chemical environment. In a structurally perfect translationally periodic crystal, the unit cell repeats exactly over the crystal, and the number of lines in the NMR spectrum is determined by the number of different local chemical environments of the resonant nuclei in the unit cell. Due to the exact repetition of the local chemical environments over the unit cells, the lines in the NMR spectrum of a perfect crystal are sharp. In crystals containing disorder, local chemical environments no more repeat exactly over the unit cells, so that the resonance frequencies

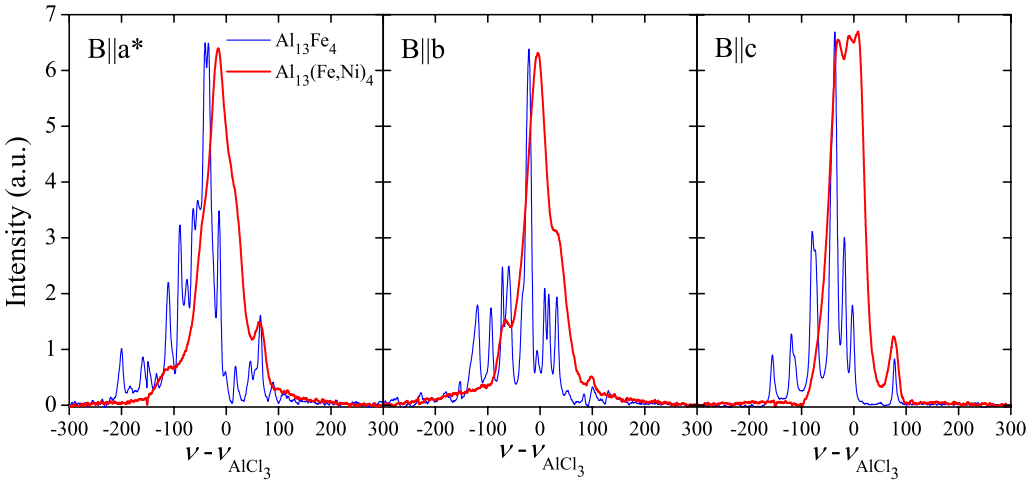

FIG. 2. (Color online) ^{27}Al NMR spectra of the $Al_{13}Fe_4$ and $Al_{13}(Fe,Ni)_4$ single crystals for the magnetic field oriented along the a^*, b, and c crystallographic directions. The spectra were recorded in a magnetic field $B=9.39$ T at the temperature 80 K. The frequency origin is taken at the ^{27}Al resonance of the $AlCl_3$ aqueous solution ($\nu_{AlCl_3}=104.223$ MHz).

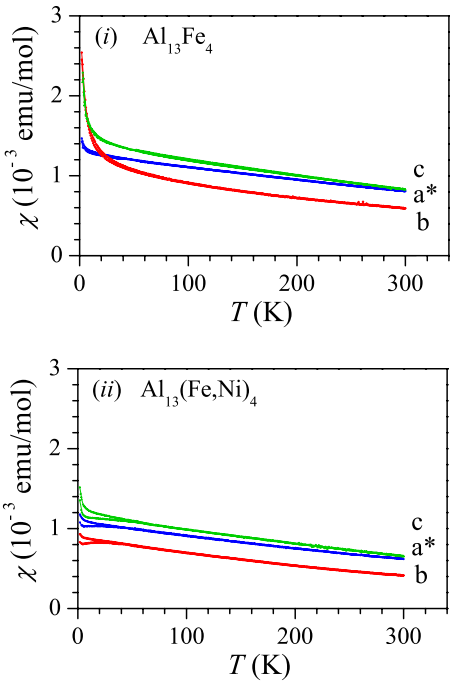

FIG. 3. (Color online) Temperature-dependent magnetic susceptibility $\chi=M/H$ of (i) $Al_{13}Fe_4$ and (ii) $Al_{13}(Fe,Ni)_4$ in the field $H=1$ kOe applied along the a^*, b, and c crystallographic directions. Both zfc and fc runs were performed. The zfc-fc susceptibility splitting [more pronounced for the $Al_{13}(Fe,Ni)_4$] is observed below about 40 K, where the lower branch always represents χ_{zfc} and the upper branch is χ_{fc}.

become smeared, the individual lines in the spectrum become inhomogeneously broadened and the structure of sharp lines is replaced by a more or less featureless single broad line. This is indeed observed in Fig. 2, where the broad spectrum of $Al_{13}(Fe,Ni)_4$ replaces the sharp structure of the $Al_{13}Fe_4$ spectrum, demonstrating that the $Al_{13}(Fe,Ni)_4$ can be viewed as a disordered version of the structurally well-ordered $Al_{13}Fe_4$. Further details of the structure of the $Al_{13}Fe_4$ spectrum in terms of the number of NMR lines, their intensities and positions on the frequency axis as a function of the crystal orientation in the magnetic field, in relation to the structure of the unit cell, are beyond the scope of this paper.

B. Magnetization and magnetic susceptibility

The temperature-dependent magnetic susceptibility, $\chi(T)$, and the magnetization as a function of the magnetic field, $M(H)$, were investigated in the temperature interval between 300 and 2 K, using Quantum Design MPMS XL-5 superconducting quantum interference device magnetometer, equipped with a 50 kOe magnet. In the orientation-dependent measurements, magnetic field was directed along the long axis of each sample, thus along the a^*, b, and c crystallographic directions. The susceptibility $\chi(T)$, measured in a field of 1 kOe, is displayed in Fig. 3(i) for $Al_{13}Fe_4$ and in Fig. 3(ii) for $Al_{13}(Fe,Ni)_4$. Both zero-field-cooled (zfc) and field-cooled (fc) temperature runs were performed. A zfc-fc susceptibility splitting [more pronounced for the $Al_{13}(Fe,Ni)_4$] is observed below about 40 K, demonstrating the presence of a remnant spin fraction. In the high-temperature regime above 40 K, the orientation-dependent susceptibilities of the $Al_{13}(Fe,Ni)_4$ show linearlike increase with decreasing temperature. The susceptibilities of the $Al_{13}Fe_4$ are of Curie type, exhibiting $1/T$—like dependence on cooling as characteristic of localized paramagnetic spins. The susceptibility values at 300 K, being around 1×10^{-3} emu/mol for both investigated compounds and all crystallographic directions, are one to two orders of magnitude larger than the (absolute) diamagnetic core susceptibility, estimated from literature tables[29] to be in the range $\chi_{dia}=[-6.6,-7.8]\times10^{-5}$ emu/mol for different ionization states of the constituent elements [since the diamagnetic contribution of Ni^{2+} is almost the same as that of Fe^{2+} and Fe^{3+}, there is practically no difference between the χ_{dia} of $Al_{13}Fe_4$ and $Al_{13}(Fe,Ni)_4$]. The orientation-dependent susceptibilities of $Al_{13}(Fe,Ni)_4$ are smaller from the corresponding susceptibilities of $Al_{13}Fe_4$. Further discussion of different contributions to the magnetization of $Al_{13}Fe_4$ and $Al_{13}(Fe,Ni)_4$ will be given in the $M(H)$ analysis, to be presented in the following. Regarding the anisotropy of the susceptibility, it is the same for both compounds above 40 K, appearing in the order $\chi_b<\chi_{a^*}<\chi_c$. The susceptibility is the lowest for the magnetic field along the stacking b direction, whereas the anisotropy between the two in-plane directions a^* and c is very small. While in the $Al_{13}(Fe,Ni)_4$ this order of anisotropy is preserved down to the lowest investigated temperature, χ_{a^*}, χ_b, and χ_c of $Al_{13}Fe_4$ exhibit quite different temperature-dependent increase below 40 K by crossing each other, so that the order of anisotropy is changed below that temperature.

The $M(H)$ curves at $T=5$ K are displayed in Fig. 4(i) for the $Al_{13}Fe_4$ and in Fig. 4(ii) for the $Al_{13}(Fe,Ni)_4$. For both compounds and all three directions, the $M(H)$ dependence is positive paramagnetic. In the close vicinity of $H=0$, all $M(H)$ curves show a small hysteresis loop that saturates already in the field of 1 kOe. The hysteresis loop for the field along the a^* direction of $Al_{13}Fe_4$ is shown on an expanded scale in the inset of Fig. 4(i). These loops identify a small ferromagnetic (FM) component in the magnetization of both compounds and will be quantified in the subsequent analysis. Away from the $H\rightarrow0$ hysteretic region, the $M(H)$ curves of $Al_{13}(Fe,Ni)_4$ are linearlike for all three directions, whereas in the case of $Al_{13}Fe_4$, the magnetization curves are slightly curved as typical for the presence of localized paramagnetic spins. For all directions, the magnetization of $Al_{13}Fe_4$ is larger from that of $Al_{13}(Fe,Ni)_4$, in agreement with the susceptibility results of Fig. 3. The anisotropy of the magnetization is also in agreement with the susceptibility anisotropy at 5 K of Fig. 3.

The experimental $M(H)$ curves of $Al_{13}(Fe,Ni)_4$ were reproduced theoretically by the expression

$$M = M_0 L(\mu H/k_B T) + kH. \quad (1)$$

The first term describes the FM contribution, where M_0 is the saturated magnetization and $L(x)=\coth(x)-1/x$ is the Langevin function that is a limit of the Brillouin function for large

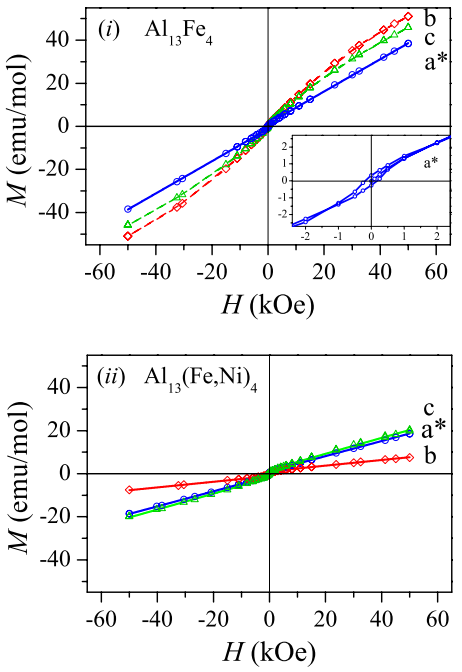

FIG. 4. (Color online) The $M(H)$ curves at $T=5$ K of (i) $Al_{13}Fe_4$ and (ii) $Al_{13}(Fe,Ni)_4$ for the field applied along the a^*, b, and c crystallographic directions. An expanded portion of the $M(H)$ curve of $Al_{13}Fe_4$ around $H=0$ for the a^* direction, showing the hysteresis loop, is shown in the inset of panel (i). Solid curves are fits with Eq. (1) (except in the inset) whereas dashed lines are guides for the eyes.

magnetic moments μ. The Langevin function reproduces well the average curvature of the FM hysteresis loop around the $H=0$ origin, but with an unphysically large magnetic moment μ, so that its relevance is merely to enable extraction of the second term, kH, from the total magnetization (note, however, that the M_0 parameter is well defined). Here k represents terms in the susceptibility $\chi=M/H$ that are linear in the magnetic field (the Larmor core diamagnetic susceptibility and the susceptibility of the conduction electrons—the Pauli spin paramagnetic contribution and the Landau orbital diamagnetic contribution). In the case that small localized magnetic moments on the order of 0.1 Bohr magneton μ_B are present as well (e.g., the paramagnetic Fe or Ni moments that are partially screened by the conduction electron cloud in an electrically conducting environment), these also give linear $M(H)$ response in the investigated field range up to 50 kOe (recall that the expansion of the Brillouin function for small magnetic moments is linear with the field) and are thus also included in k.

The fits with Eq. (1) of the $Al_{13}(Fe,Ni)_4$ $M(H)$ curves are shown by solid curves in Fig. 4(ii). For the a^* direction, the following fit parameter values were obtained: $\mu=204\mu_B$, $M_0=1.2$ emu/mol$=5\times10^{-5}\mu_B$/atom Fe (and Ni), and $k=3.6\times10^{-4}$ emu/mol. Very similar μ and M_0 values were obtained also for the other two directions. The k value for the c direction was also almost identical to that for the a^* direction, whereas for the b direction it amounted $k=1.4\times10^{-4}$ emu/mol, owing to the smaller slope of the $M(H)$ curve for this direction. The microscopic origin of the FM component is not clear, but similar FM contributions to the magnetization were reported also for the related decagonal approximants [Y-Al-Ni-Co (Ref. 12) and o-$Al_{13}Co_4$ (Ref. 14)] and d-QCs [d-$Al_{72}Ni_{12}Co_{16}$ (Ref. 30) and d-$Al_{70}Ni_{15}Co_{15}$ (Ref. 31)], where it was suggested that they could originate from the transition-metal-rich regions in the samples. Here it is important to note that both the original and the refined structural models of the $Al_{13}Fe_4$ phase do not contain any Fe-rich domains, so that the experimentally detected FM contribution should be associated with defects in the crystal, either FM impurities in ppm concentrations in the starting materials, or more likely, the FM iron-oxide phases at the samples' surfaces. Considering the second possibility, the FM fraction in the $Al_{13}(Fe,Ni)_4$ samples can be estimated from the fit-determined M_0 value by comparing to the known M_0 values of typical iron-oxide compounds. For the magnetite Fe_3O_4, the literature-reported value is $M_0=1.33\mu_B$/atom Fe and the values for other iron oxides are similar. This yields the FM fraction in $Al_{13}(Fe,Ni)_4$ of 4.0×10^{-5} of all Fe (and Ni) atoms. This value is too large to be associated with the FM impurities in the starting materials, so that the FM surface iron oxides should be considered as the origin of the FM component in the magnetization. The surface iron oxides in Fe-containing intermetallic compounds are inevitable at ambient conditions; if polished away, they reappear almost instantly in the air atmosphere.

Analyzing the $M(H)$ curves of the $Al_{13}Fe_4$ from Fig. 4(i), the fitting function of Eq. (1) that contains the Langevin function and the linear term was no more adequate due to the continuous curvature of the $M(H)$ curves up to the highest investigated field. In this case, the Brillouin function should be added to Eq. (1), but then the number of fit parameters becomes too large to obtain reliable fits and we skipped this kind of analysis. We have nevertheless performed the analysis with Eq. (1) for the a^* direction of $Al_{13}Fe_4$ [solid curve in Fig. 4(i)], where the $M(H)$ experimental data still show linearlike behavior at fields above 10 kOe. The obtained fit parameter values are $\mu=106\mu_B$, $M_0=1.3$ emu/mol$=6\times10^{-5}\mu_B$/atom Fe, and $k=7.5\times10^{-4}$ emu/mol. The M_0 value then yields the FM fraction in $Al_{13}Fe_4$ of 4.5×10^{-5} of all Fe atoms, a value that is practically identical to that determined for the $Al_{13}(Fe,Ni)_4$.

C. Electrical resistivity

Electrical resistivity was measured between 300 and 2 K using the standard four-terminal technique. The $\rho(T)$ data along the three crystallographic directions are displayed in Fig. 5(i) for the $Al_{13}Fe_4$ and in Fig. 5(ii) for the $Al_{13}(Fe,Ni)_4$. For both compounds, the anisotropic resistivities appear in the order $\rho_b<\rho_{a^*}<\rho_c$, so that the resistivity is the lowest along the stacking b direction perpendicular to the atomic planes. The anisotropy between the two in-plane directions a^* and c is also substantial.

The resistivities of the two compounds exhibit different temperature dependence. $Al_{13}Fe_4$ exhibits small residual resistivities $\rho(T\rightarrow0)$, amounting at 2 K $\rho_{a^*}^{2\ \mathrm{K}}=11$ $\mu\Omega$ cm, $\rho_b^{2\ \mathrm{K}}=2.5$ $\mu\Omega$ cm, and $\rho_c^{2\ \mathrm{K}}=14$ $\mu\Omega$ cm, and large PTC of the resistivity along all three crystallographic directions,

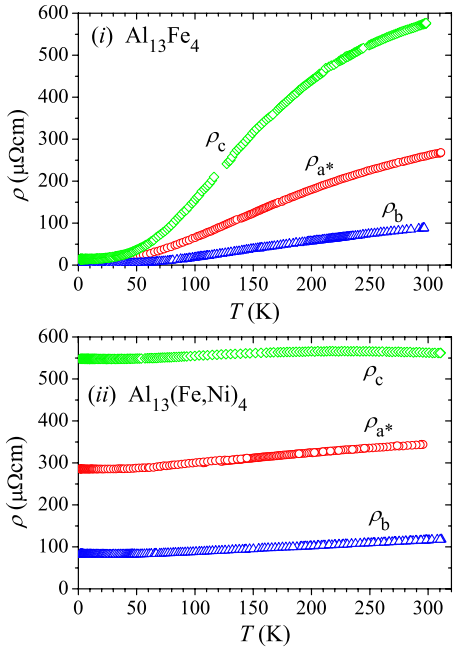

FIG. 5. (Color online) Temperature-dependent electrical resistivity of (i) $Al_{13}Fe_4$ and (ii) $Al_{13}(Fe,Ni)_4$ along three orthogonal crystallographic directions a^*, b, and c.

demonstrating an important role of the electron-phonon scattering mechanism. At 300 K, the resistivities reach the values $\rho_{a^*}^{300\ K}=268\ \mu\Omega$ cm, $\rho_b^{300\ K}=88\ \mu\Omega$ cm, and $\rho_c^{300\ K}=576\ \mu\Omega$ cm. In contrast, the residual resistivities of $Al_{13}(Fe,Ni)_4$ are much larger, amounting $\rho_{a^*}^{2\ K}=286\ \mu\Omega$ cm, $\rho_b^{2\ K}=81\ \mu\Omega$ cm, and $\rho_c^{2\ K}=548\ \mu\Omega$ cm, and the PTC of the resistivity is small for all three crystallographic directions. The 300 K resistivity values of $Al_{13}(Fe,Ni)_4$ are almost the same as those of $Al_{13}Fe_4$. The marked difference between the residual resistivities of the two compounds can be explained by the presence of quenched structural disorder in the $Al_{13}(Fe,Ni)_4$ and its absence in the $Al_{13}Fe_4$. Within the relaxation-time approximation, the electrical resistivity of a solid is proportional to the inverse relaxation time τ of the conduction electrons between two scattering events, $\rho \propto 1/\tau$. Assuming a nonmagnetic solid, the relaxation rate contains two terms, $1/\tau = 1/\tau_0 + 1/\tau_{ph}$, where $1/\tau_0$ describes elastic scattering of electrons by quenched defects and $1/\tau_{ph}$ is due to electron-phonon inelastic scattering. In a perfect structure, the absence of quenched disorder implies $1/\tau_0 = 0$, whereas the phonon rate vanishes in the limit $T \to 0$, so that the total rate $1/\tau$ vanishes at zero temperature and the residual resistivity is zero in this limit. In the presence of quenched disorder, $1/\tau_0 \neq 0$ and the residual $T \to 0$ resistivity is nonzero. In the structurally well-ordered $Al_{13}Fe_4$, the amount of quenched disorder is small, yielding small residual resistivities and large PTC due to the high density of phonons in the lattice that are at the origin of the PTC. The large nonzero residual resistivity of $Al_{13}(Fe,Ni)_4$ is, on the other hand, a consequence of quenched disorder in this compound. The strong anisotropy of the residual resistivity suggests that the amount of quenched disorder depends on the crystallographic direction.

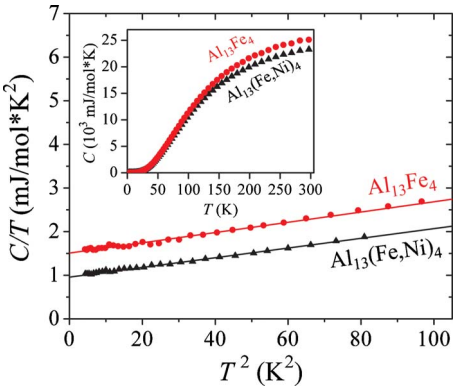

FIG. 6. (Color online) Low-temperature molar specific heats of the $Al_{13}Fe_4$ and $Al_{13}(Fe,Ni)_4$ in a C/T versus T^2 plot. The specific heats in the entire investigated temperature range (2–300 K) are displayed in the inset. The figures are calculated per mol of $Al_{0.765}Fe_{0.235}$ "molecules" for $Al_{13}Fe_4$ and mol of $Al_{0.765}Fe_{0.235}Ni_{0.022}$ for $Al_{13}(Fe,Ni)_4$.

Structural disorder also explains the small PTC of the resistivity in this compound, as the disorder suppresses propagation of phonons. However, the nonzero PTC of the resistivity in the disordered $Al_{13}(Fe,Ni)_4$ demonstrates that structural disorder does not suppress the phonons completely, but some phonons are still excited, though their density is considerably smaller from that in the structurally well-ordered $Al_{13}Fe_4$.

D. Specific heat and the electronic density of states at ε_F

The low-temperature specific heat $C(T)$ is a convenient quantity to estimate the value of the electronic density of states (DOS) at the Fermi energy ε_F and the Debye temperature θ_D. In nonmagnetic metals and metallic compounds, the total specific heat is a sum of the electronic and lattice specific heats. The electronic specific heat depends linearly on temperature, $C_{el}(T) = \gamma T$, with the electronic specific-heat coefficient $\gamma = (\pi^2/3)k_B^2 g(\varepsilon_F)$, where $g(\varepsilon_F)$ is the DOS at ε_F. At low temperatures below about 10 K, the lattice specific heat can usually be well approximated by the Debye model and is expressed as a function of temperature in the form $C_{latt}(T) = \alpha T^3$. The lattice specific-heat coefficient α is related to the Debye temperature via the relation $\theta_D = (12\pi^4 R/5\alpha)^{1/3}$, where R is the gas constant. The total specific heat at low temperatures can then be written as

$$C(T) = \gamma T + \alpha T^3. \quad (2)$$

In order to extract γ and α, Eq. (2) is usually rewritten in the form $C/T = \gamma + \alpha T^2$. Plotting the low-temperature C/T data versus T^2 yields a straight line with the intercept γ and the slope α.

Specific-heat measurements were performed in the temperature range between 2 and 300 K by using a Quantum Design physical property measurement system (PPMS) that employs a thermal-relaxation calorimeter. Specific heat of the Al metal (99.998% purity) was determined for reference. The low-temperature molar specific heats of the $Al_{13}Fe_4$ and the $Al_{13}(Fe,Ni)_4$ are displayed in Fig. 6 in a C/T versus T^2

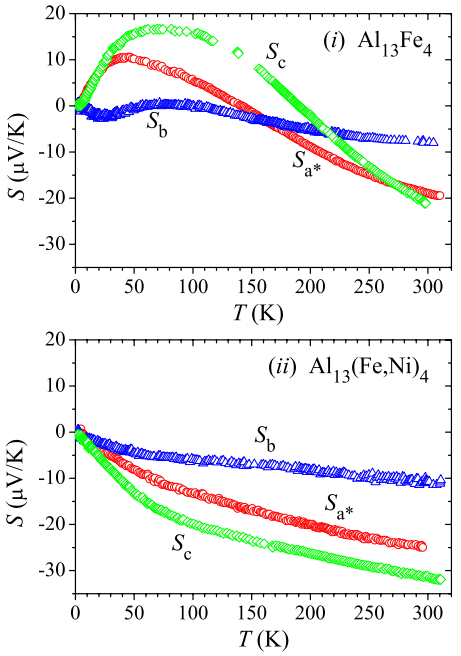

FIG. 7. (Color online) Temperature-dependent thermoelectric power (the Seebeck coefficient S) of (i) $Al_{13}Fe_4$ and (ii) $Al_{13}(Fe,Ni)_4$ along three orthogonal crystallographic directions a^*, b, and c.

plot, whereas the specific heats in the entire investigated temperature range are displayed in the inset. For the $Al_{13}Fe_4$, the analysis yielded the values $\gamma_{Al_{13}Fe_4}=1.51$ mJ/mol K^2 and $\theta_D^{Al_{13}Fe_4}=544$ K whereas for the $Al_{13}(Fe,Ni)_4$ the values are $\gamma_{Al_{13}(Fe,Ni)_4}=0.98$ mJ/mol K^2 and $\theta_D^{Al_{13}(Fe,Ni)_4}=564$ K. The reference values for the Al metal (the graph is not shown) are $\gamma_{Al}=1.53$ mJ/mol K^2 and $\theta_D^{Al}=410$ K, in agreement with the literature data.[32] The above γ values allow estimating the value of the DOS g at ε_F relative to the Al metal. For the $Al_{13}Fe_4$ we obtain $\gamma_{Al_{13}Fe_4}/\gamma_{Al}=g_{Al_{13}Fe_4}/g_{Al}=0.99$, whereas for the $Al_{13}(Fe,Ni)_4$ the ratio is $\gamma_{Al_{13}(Fe,Ni)_4}/\gamma_{Al}=g_{Al_{13}(Fe,Ni)_4}/g_{Al}=0.64$. For both compounds, the DOS at ε_F is metallic high. While for the $Al_{13}Fe_4$ the DOS at ε_F value is practically the same as that of the Al metal, the DOS of the $Al_{13}(Fe,Ni)_4$ is reduced to 64%, which can be attributed to the effect of structural and substitutional disorder in this compound.

E. Thermoelectric power

The thermoelectric power (the Seebeck coefficient S) was measured between 300 and 2 K by using a standard temperature-gradient technique. The thermopower data, measured along the three crystallographic directions a^*, b, and c, are displayed in Fig. 7(i) for the $Al_{13}Fe_4$ and in Fig. 7(ii) for the $Al_{13}(Fe,Ni)_4$. We first discuss the thermopower of the disordered $Al_{13}(Fe,Ni)_4$. The thermopower of this compound is negative for all three directions, suggesting that electron-type carriers dominate the thermoelectric transport. The RT values are in the range between −10 and −32 μV/K with the order of anisotropy $|S_c|>|S_{a^*}|>|S_b|$. The temperature dependence of $S(T)$ is qualitatively similar for all three directions. It changes monotonously with increasing temperature and a change in slope is observed at about 70 K, where the low-temperature slope is higher than the high-temperature one. Nonlinearities in the thermopower in this temperature range are often associated with electron-phonon effects, which typically reach their maximum value at a temperature that is some fraction of the Debye temperature θ_D. The thermopower in all three directions extrapolates approximately linearly to zero upon $T\rightarrow 0$, a feature that is usually associated with metallic diffusion thermopower. These features allow assigning the $S(T)$ data from Fig. 7(ii) to the behavior expected for the electron-phonon enhancement of diffusion thermopower. The same behavior was observed in the thermopower of the related Y-Al-Ni-Co (Ref. 12) decagonal approximant and the d-$Al_{73}Co_{10}Ni_{17}$ quasicrystal,[33] as well as for several metallic glasses.[34] The role of phonons in the temperature-dependent thermopower of $Al_{13}(Fe,Ni)_4$ is analogous to their role in the temperature-dependent electrical resistivity of this compound [Fig. 5(ii)], where the electron-phonon scattering is responsible for the small PTC of the resistivity.

The temperature dependence of the anisotropic thermopower of $Al_{13}Fe_4$ shown in Fig. 7(i) is more complicated. The thermopowers along different crystallographic directions exhibit maxima, crossovers and also change sign. Assuming that the electronic DOS does not exhibit sharp features in the vicinity of the Fermi energy ε_F, such complicated behavior may originate from (1) specific details of the anisotropic Fermi surface that contains electronlike and holelike parts and (2) anisotropic electron-phonon interactions, which are stronger in the structurally ordered $Al_{13}Fe_4$ compound as compared to the disordered $Al_{13}(Fe,Ni)_4$ due to the higher density of phonons (as also evident from the strong PTC of the resistivity of $Al_{13}Fe_4$).

F. Hall coefficient

The Hall-coefficient measurements were performed by the five-point method using standard ac technique in magnetic fields up to 10 kOe. The current through the samples was in the range 10–50 mA. The measurements were performed in the temperature interval from 90 to 370 K. The anisotropic temperature-dependent Hall coefficient $R_H=E_y/j_xB_z$ of $Al_{13}Fe_4$ is shown in Fig. 8(i), whereas R_H of $Al_{13}(Fe,Ni)_4$ is shown in Fig. 8(ii). In order to determine the anisotropy of R_H, three sets of experiments were performed with the current j_x along the long axis of each sample (thus along a^*, b, and c, respectively), whereas the magnetic field B_z was directed along each of the other two orthogonal crystallographic directions, making six experiments altogether for each compound. For all combinations of directions, the R_H values are typical metallic in the range 10^{-9}–10^{-10} m^3 C^{-1} (with the experimental uncertainty of $\pm 0.1\times 10^{-10}$ m^3 C^{-1}). R_H's exhibit pronounced anisotropy with the following regularity. The six R_H sets of data form three groups of two practically identical R_H curves, where the magnetic field in a given crystallographic direction yields the same R_H for the current along the other two crystallographic directions in the perpendicular plane. Thus, identical Hall coefficients are ob-

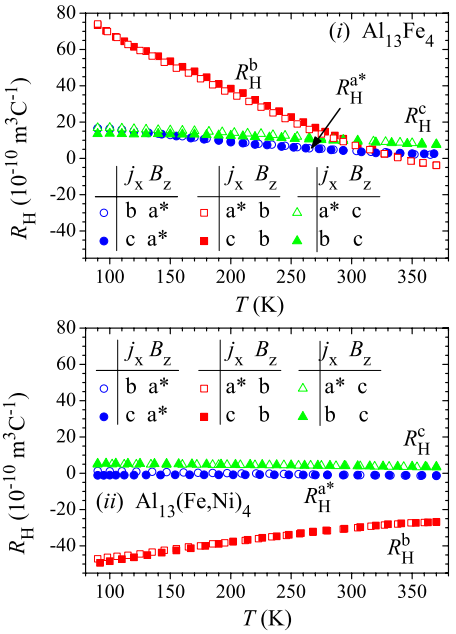

FIG. 8. (Color online) Anisotropic temperature-dependent Hall coefficient $R_H=E_y/j_xB_z$ of (i) $Al_{13}Fe_4$ and (ii) $Al_{13}(Fe,Ni)_4$ for different combinations of directions of the current j_x and magnetic field B_z (given in the legend). The superscript a^*, b, or c on R_H denotes the direction of the magnetic field.

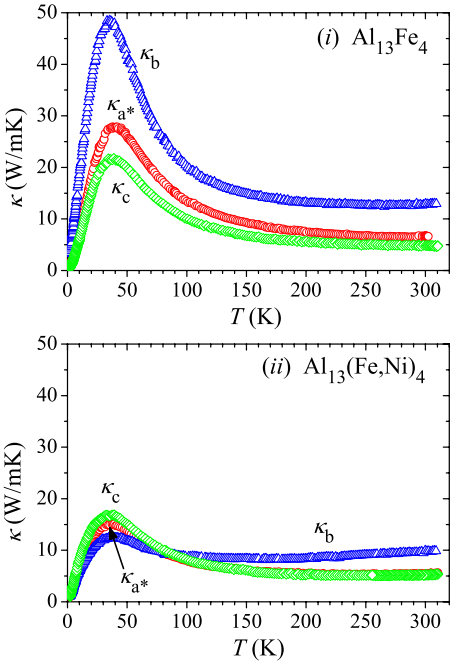

FIG. 9. (Color online) Total thermal conductivity κ of (i) $Al_{13}Fe_4$ and (ii) $Al_{13}(Fe,Ni)_4$ along three orthogonal crystallographic directions a^*, b, and c.

tained for the pair combinations $E_b/j_cB_{a^*}=E_c/j_bB_{a^*}=R_H^{a^*}$ (where the additional superscript on the Hall coefficient denotes the direction of the magnetic field), $E_{a^*}/j_cB_b=E_c/j_{a^*}B_b=R_H^b$ and $E_b/j_{a^*}B_c=E_{a^*}/j_bB_c=R_H^c$. At 100 K, the anisotropic R_H values of the $Al_{13}Fe_4$ amount $R_H^{a^*}=1.7\times10^{-9}$ m^3 C^{-1}, $R_H^b=6.8\times10^{-9}$ m^3 C^{-1}, and $R_H^c=1.6\times10^{-9}$ m^3 C^{-1} whereas the corresponding values of the $Al_{13}(Fe,Ni)_4$ are $R_H^{a^*}=-1.1\times10^{-10}$ m^3 C^{-1}, $R_H^b=-4.6\times10^{-9}$ m^3 C^{-1}, and $R_H^c=4.9\times10^{-10}$ m^3 C^{-1}. For both compounds, $R_H^{a^*}$ and R_H^c are almost temperature independent within the investigated temperature range whereas R_H^b shows quite strong temperature dependence, being positive in the $Al_{13}Fe_4$ and negative in the $Al_{13}(Fe,Ni)_4$.

The Hall coefficients of the $Al_{13}Fe_4$ and the $Al_{13}(Fe,Ni)_4$ show complicated temperature-dependent anisotropy for different combinations of the current and field directions. For some combinations, the Hall coefficient is electronlike ($R_H<0$), for others it is holelike ($R_H>0$) or practically zero [e.g., $R_H^{a^*}$ of $Al_{13}(Fe,Ni)_4$]. The R_H^c of $Al_{13}Fe_4$ even changes sign with temperature at $T=350$ K. All this reflects complicated structure of the anisotropic Fermi surface that contains electronlike and holelike contributions. Depending on the combination of crystallographic directions, either electronlike ($R_H<0$) or holelike ($R_H>0$) contributions dominate, or the two contributions compensate each other ($R_H\approx0$). Quantitative analysis is difficult and requires knowledge of the anisotropic Fermi surface. Here we note that similar complicated Hall-coefficient anisotropy was reported also for the related decagonal approximants Y-Al-Ni-Co (Refs. 12 and 13) and o-$Al_{13}Co_4$ (Ref. 14). For the Y-Al-Ni-Co, this anisotropy was quantitatively reproduced theoretically by an *ab initio* calculation using the anisotropic Fermi surface of this compound.[13]

G. Thermal conductivity

Thermal conductivity κ was measured along the a^*, b, and c directions using an absolute steady-state heat-flow method. The thermal flux through the samples was generated by a 1 kΩ RuO_2 chip resistor, glued to one end of the sample while the other end was attached to a copper heat sink. The temperature gradient across the sample was monitored by a chromel-constantan differential thermocouple. The total thermal conductivity κ along the three crystallographic directions is displayed in Fig. 9(i) for the $Al_{13}Fe_4$ and in Fig. 9(ii) for the $Al_{13}(Fe,Ni)_4$. For both compounds and all three directions, κ shows a typical phonon *umklapp* maximum at about 35 K. In $Al_{13}Fe_4$, the thermal conductivity shows large anisotropy in the order $\kappa_b>\kappa_{a^*}>\kappa_c$, being the highest along the stacking b direction, whereas the in-plane conductivities κ_{a^*} and κ_c are lower and show smaller, yet significant anisotropy. Since the electrical conductivity $\sigma(T)=\rho^{-1}(T)$ of $Al_{13}Fe_4$ [Fig. 5(i)] is also the highest along b, this material is the best conductor for both the electricity and heat along the stacking b direction perpendicular to the (a,c) atomic planes. In the $Al_{13}(Fe,Ni)_4$, on the other hand, the anisotropy of the thermal conductivity between the stacking b and the in-plane a^* and c directions is small, whereas there is practically no anisotropy between the two in-plane directions. An important difference between the thermal conductivities of the two investigated compounds are the significantly larger conductivity values in the structurally ordered $Al_{13}Fe_4$, as compared to the disordered $Al_{13}(Fe,Ni)_4$. For example, the κ_b conductivity of $Al_{13}Fe_4$ at the umklapp maximum at 35 K is by a factor

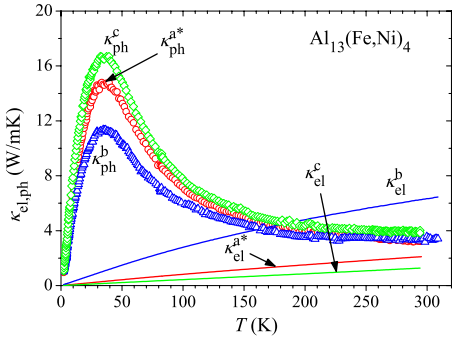

FIG. 10. (Color online) Electronic contribution κ_{el} (solid curves), estimated from the Wiedemann-Franz law, and phononic contribution $\kappa_{ph}=\kappa-\kappa_{el}$ (symbols) to the total thermal conductivity κ of $Al_{13}(Fe,Ni)_4$ along three orthogonal crystallographic directions a^*, b, and c.

4 larger from the corresponding value of $Al_{13}(Fe,Ni)_4$. This reduction in the thermal conductivity in the disordered $Al_{13}(Fe,Ni)_4$ gets simple explanation by considering the disorder-induced suppression of the electron and phonon propagation in the crystalline lattice. The two effects will be elaborated in more detail in the following by analyzing the electronic and phononic parts of the total thermal conductivity.

The phononic contribution $\kappa_{ph}=\kappa-\kappa_{el}$ can be estimated by subtracting the electronic contribution κ_{el} from the total conductivity κ using the Wiedemann-Franz (WF) law, $\kappa_{el}=\pi^2k_B^2T\sigma(T)/3e^2$, and the measured electrical conductivity data $\sigma(T)$. Here it is important to recall the validity of the WF law,[35] which is valid under the condition of dominant elastic scattering of the electrons, usually realized at high temperatures $T>\theta_D$ (e.g., for typical metals, the WF law is valid already at RT). At low temperatures, the WF law is valid for solids where only the residual electrical resistivity (due to elastic scattering by quenched defects) is observed. Inspecting the electrical resistivities of the $Al_{13}Fe_4$ and $Al_{13}(Fe,Ni)_4$ from Fig. 5, we observe that the residual resistivity is the dominant part of the total resistivity of the disordered $Al_{13}(Fe,Ni)_4$ within the investigated temperature range 2–300 K, so that the WF law should be a good approximation to $\kappa_{el}(T)$ of this compound. For the structurally ordered $Al_{13}Fe_4$, on the other hand, the residual resistivities are very small, and the WF law can be used only at high temperatures, such as RT and above. For that reason we present in the following the analysis of κ_{el} and κ_{ph} of the $Al_{13}(Fe,Ni)_4$ in the entire investigated temperature range, whereas for the $Al_{13}Fe_4$, we present only the 300 K κ_{el} and κ_{ph} values.

The κ_{el} (solid curves) and κ_{ph} (symbols) contributions to the total thermal conductivity of $Al_{13}(Fe,Ni)_4$ are shown in Fig. 10. The electronic contribution shows anisotropy in the order $\kappa_{el}^b>\kappa_{el}^{a^*}>\kappa_{el}^c$, where the anisotropy between the stacking b and the in-plane (a^*,c) directions is large, whereas the in-plane anisotropy is much smaller. At 300 K, we obtain the values $\kappa_{el}^{a^*}=2.1$ W/mK, $\kappa_{el}^b=6.3$ W/mK, and $\kappa_{el}^c=1.3$ W/mK. Since the total thermal conductivities at 300 K amount $\kappa_{a^*}=5.4$ W/mK, $\kappa_b=9.9$ W/mK, and $\kappa_c=5.1$ W/mK, this gives the ratios $(\kappa_{el}^{a^*}/\kappa_{a^*})_{300\ K}=0.39$, $(\kappa_{el}^b/\kappa_b)_{300\ K}=0.64$, and $(\kappa_{el}^c/\kappa_c)_{300\ K}=0.25$. Electrons (and holes) are thus significant, yet not the dominant heat carriers at 300 K, showing the importance of phonons for the heat transport in the $Al_{13}(Fe,Ni)_4$. The phononic contribution κ_{ph} is also anisotropic (Fig. 10), but the anisotropy tends to disappear at elevated temperatures.

For the structurally ordered $Al_{13}Fe_4$, we obtain the following electronic thermal conductivity values at 300 K: $\kappa_{el}^{a^*}=2.8$ W/mK, $\kappa_{el}^b=8.3$ W/mK, and $\kappa_{el}^c=1.3$ W/mK, whereas the total conductivities are $\kappa_{a^*}=6.7$ W/mK, $\kappa_b=12.8$ W/mK, and $\kappa_c=4.7$ W/mK. This gives the ratios $(\kappa_{el}^{a^*}/\kappa_{a^*})_{300\ K}=0.42$, $(\kappa_{el}^b/\kappa_b)_{300\ K}=0.65$, and $(\kappa_{el}^c/\kappa_c)_{300\ K}=0.28$, which are almost identical values as those obtained for the $Al_{13}(Fe,Ni)_4$.

IV. DISCUSSION

In an anisotropic crystal, the transport coefficients are generally tensors, depending on the crystallographic direction. For example, the electrical conductivity $\boldsymbol{\sigma}$ (the inverse resistivity $\boldsymbol{\rho}^{-1}$) is a symmetric (and diagonalizable) second-rank tensor, relating the current density $\vec{j}$ to the electric field $\vec{E}$ via the relation $j_i=\Sigma_j\sigma_{ij}E_j$, where $i,j=x,y,z$ denote crystallographic directions. The geometry of our samples (their long edges were along three orthogonal directions a^*, b, and c and the electric field or the temperature gradient were applied along their long edges) imply that diagonal elements of the electrical conductivity, the thermoelectric power, and the thermal conductivity tensors were measured in a Cartesian x,y,z coordinate system (e.g., the elements $\sigma_{xx}=\sigma_{a^*}$, $\sigma_{yy}=\sigma_b$, and $\sigma_{zz}=\sigma_c$ of the conductivity tensor or the elements $S_{xx}=S_{a^*}$, $S_{yy}=S_b$, and $S_{zz}=S_c$ of the thermopower tensor were experimentally determined). Due to the monoclinic symmetry of the $Al_{13}Fe_4$ and the $Al_{13}(Fe,Ni)_4$ unit cells, the above tensors are not diagonal in this system.

In order to perform quantitative theoretical analysis of the anisotropic transport coefficients, evaluation of the tensor elements requires knowledge of the anisotropic Fermi surface. We have calculated the Fermi surface of the $Al_{13}Fe_4$ for the refined structural model. The *ab initio* calculation of the electronic band structure $\varepsilon_{\vec{k},n}$ (where n is the band index) was performed within the framework of the density-functional theory. We applied the ABINIT (Ref. 36) code and the local-density approximation[37] for the exchange-correlation potential. The electron-ion interactions were described with the norm-conserving pseudopotentials[38] of the Troullier-Martins[39] type. Due to a relatively large number of atoms (102) in the unit cell, the plane-wave cut-off parameter ε_{cut} was limited to 220 eV, whereas, according to the tests, $N_{\vec{k}}=168$ $\vec{k}$ points in the full Brillouin zone were enough to obtain a dense mesh of the energy eigenvalues $\varepsilon_{\vec{k},n}$. The *ab initio* calculated Fermi surface, visualized by using the XCRYSDEN program,[40] is presented in Fig. 11. There are six bands crossing the Fermi energy ε_F, resulting in a significant complexity. It is transparent that the Fermi surface is highly anisotropic, which is at the origin of the experimentally ob-

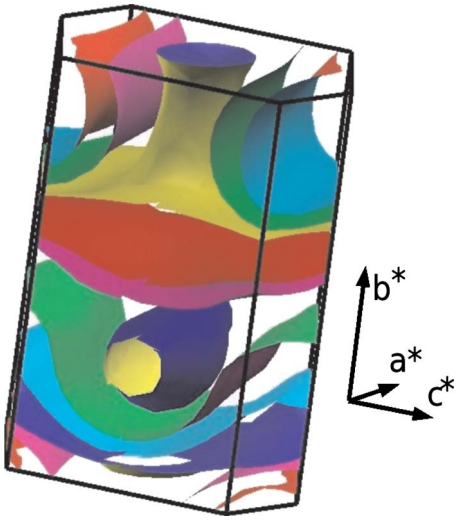

FIG. 11. (Color online) Fermi surface in the first Brillouin zone, calculated *ab initio* for the refined structural model of $Al_{13}Fe_4$. Orientation of the reciprocal-space axes a^*, b^*, and c^* is also shown.

served anisotropy in the electronic transport coefficients along different crystallographic directions.

In the next step, an attempt was made to calculate the anisotropic temperature-dependent transport coefficients by means of the Boltzmann semiclassical theory, using the BOLTZTRAP code[41] and the theoretical Fermi surface from Fig. 11. The details of calculations are identical to those outlined in our previous work on the related Y-Al-Ni-Co and o-$Al_{13}Co_4$ decagonal approximants.[12–14] However, for the $Al_{13}Fe_4$ the matching between the *ab initio* calculated transport coefficients and the experiment was not satisfactory and the results are not presented. Here we mention that the same kind of calculation yielded quantitative agreement within the theory and experiment for the anisotropic Hall coefficient of Y-Al-Ni-Co (Ref. 13) and also reproduced qualitatively the anisotropy of the electrical resistivity, thermoelectric power, and Hall coefficient of the o-$Al_{13}Co_4$.[14] The origin of failure of this theoretical concept for the $Al_{13}Fe_4$ still has to be elaborated.

V. CONCLUSIONS

We have investigated the magnetic susceptibility, the electrical resistivity, the specific heat, the thermoelectric power, the Hall coefficient, and the thermal conductivity of the monoclinic $Al_{13}Fe_4$ and $Al_{13}(Fe,Ni)_4$. While the $Al_{13}Fe_4$ crystals are structurally well ordered, containing small amount of quenched structural disorder, the introduction of 2 at. % of Ni into the ternary solid solution $Al_{13}(Fe,Ni)_4$ creates positional and substitutional disorder. The $Al_{13}(Fe,Ni)_4$ can thus be viewed as a disordered version of the $Al_{13}Fe_4$, so that their comparison allows studying the effect of disorder on the physical properties of these complex intermetallic compounds. The main objective was to determine the crystallographic-direction-dependent anisotropy of the investigated physical parameters when measured within the (a^*,c) atomic planes, corresponding to the quasiperiodic planes in the related *d* QCs, and along the stacking *b* direction perpendicular to the planes, corresponding to the periodic direction in *d*-QCs. The electronic transport and the magnetic properties exhibit significant anisotropy. The stacking *b* direction was found to be the most conducting direction for the electricity and heat. As the electrical and thermal conductivities of the related Y-Al-Ni-Co and o-$Al_{13}Co_4$ decagonal approximants are also the highest along the stacking direction, this feature appears to be a common property of the $Al_{13}TM_4$ family of complex intermetallic compounds. The effect of quenched disorder in the $Al_{13}(Fe,Ni)_4$ is most clearly manifested in the large residual resistivity $\rho(T\rightarrow 0)$ and significantly reduced thermal conductivity of this compound, as compared to the ordered $Al_{13}Fe_4$. Specific-heat measurements revealed that the DOS at ε_F of both compounds is metallic high. The anisotropic Hall coefficient R_H reflects complicated structure of the anisotropic Fermi surface that contains electronlike and holelike contributions. Depending on the combination of directions of the current and the magnetic field, electronlike $(R_H<0)$ or holelike $(R_H>0)$ contributions dominate, or the two contributions compensate each other $(R_H\approx 0)$. Similar complicated anisotropic behavior was observed also in the thermopower. The anisotropic Fermi surface was calculated *ab initio* using the refined $Al_{13}Fe_4$ structural model. The Fermi surface is highly anisotropic, reflecting structural and chemical anisotropy of the $Al_{13}Fe_4$ and $Al_{13}(Fe,Ni)_4$ stacked-layer compounds. The anisotropy of the Fermi surface is at the origin of the anisotropic physical properties.

The $Al_{13}Fe_4$, $Al_{13}(Fe,Ni)_4$, o-$Al_{13}Co_4$, and Y-Al-Ni-Co decagonal approximant phases from the $Al_{13}TM_4$ family of intermetallic compounds exhibit anisotropic physical properties qualitatively similar to the *d*-Al-Ni-Co-type decagonal quasicrystals. The approximants and the *d*-QCs have both in common the structural detail that atomic planes are stacked periodically. The stacked-layer structure appears to be at the origin of the anisotropic physical properties, whereas the in-plane structural details (either infinite quasiperiodic order in the *d*-QCs or periodic crystalline order in the approximant phases) seem to be of marginal importance (if they are of any at all) for the anisotropic magnetic and electronic transport properties of these stacked-layer intermetallic compounds.

Finally, it is also important to emphasize the need of using single-crystalline material, when investigating the intrinsic properties of quasicrystals and their approximant phases. This is best illustrated by comparing the electrical resistivity data of our Czochralski-grown $Al_{13}Fe_4$ single crystal from Fig. 5(i) to the resistivity reported for the same $Al_{13}Fe_4$ phase, using the material in the form of oriented bundles of small crystals.[42] While the anisotropic resistivity data of our Czochralski single crystals show PTC along all three crystallographic directions and low $T=2$ K residual resistivity values in the range 2.5–14 $\mu\Omega$ cm, the in-plane resistivity data of the oriented bundles are qualitatively and quantitatively very different (see Fig. 2 of Ref. 42), by showing a NTC with an extremely high $T=2$ K value of 20 000 $\mu\Omega$ cm and an increase upon cooling from RT to 4.2 K by a factor about 5. Similar discrepancy is observed for the o-$Al_{13}Co_4$ decagonal approximant. While the anisotropic resistivity of the Czochralski-grown o-$Al_{13}Co_4$ single crystal again shows PTC along all three crystallographic directions with the low $T=2$ K residual resistivity values in the range

48–130 $\mu\Omega$ cm,[14] the resistivity data of the same o-$Al_{13}Co_4$ phase in the morphology of oriented bundles are again qualitatively and quantitatively very different [see Fig. 1a of Ref. 42]. The resistivity of the oriented bundles along the stacking direction is PTC, but of much higher magnitude to that of the Czochralski single crystal (the T=4.2 K residual resistivity of the bundles amounts 550 $\mu\Omega$ cm, compared to 48 $\mu\Omega$ cm of the Czochralski sample). The in-plane resistivity of the bundles again shows NTC with the T=4.2 K residual resistivity of 860 $\mu\Omega$ cm, compared to the PTC resistivity of the Czochralski sample with the much lower in-plane residual resistivity of 110–130 $\mu\Omega$ cm, depending on the in-plane direction. Since grain boundaries in the polygrain material always hinder the long-range electrical transport and increase the electrical resistivity, these extrinsic factors may be at the origin of the above qualitative and quantitative resistivity differences between the single-crystalline and the polygrain morphologies of the material belonging to the same phase.

ACKNOWLEDGMENTS

This work was done within the Sixth Framework EU Network of Excellence "Complex Metallic Alloys" (Contract No. NMP3-CT-2005-500140). A.S. acknowledges support of the Ministry of Science, Education and Sports of the Republic of Croatia through the Research Project No. 035-0352826-2848.

*Corresponding author; jani.dolinsek@ijs.si

[1] T. Shibuya, T. Hashimoto, and S. Takeuchi, J. Phys. Soc. Jpn. **59**, 1917 (1990).
[2] S. Martin, A. F. Hebard, A. R. Kortan, and F. A. Thiel, Phys. Rev. Lett. **67**, 719 (1991).
[3] Y.-P. Wang and D.-L. Zhang, Phys. Rev. B **49**, 13204 (1994).
[4] S.-Y. Lin, X.-M. Wang, Li Lu, D.-L. Zhang, L. X. He, and K. H. Kuo, Phys. Rev. B **41**, 9625 (1990).
[5] D.-L. Zhang, Li Lu, X.-M. Wang, S.-Y. Lin, L. X. He, and K. H. Kuo, Phys. Rev. B **41**, 8557 (1990).
[6] Y.-P. Wang, D.-L. Zhang, and L. F. Chen, Phys. Rev. B **48**, 10542 (1993).
[7] D.-L. Zhang, S.-C. Cao, Y.-P. Wang, Li Lu, X.-M. Wang, X. L. Ma, and K. H. Kuo, Phys. Rev. Lett. **66**, 2778 (1991).
[8] K. Edagawa, M. A. Chernikov, A. D. Bianchi, E. Felder, U. Gubler, and H. R. Ott, Phys. Rev. Lett. **77**, 1071 (1996).
[9] D. N. Basov, T. Timusk, F. Barakat, J. Greedan, and B. Grushko, Phys. Rev. Lett. **72**, 1937 (1994).
[10] M. Krajčí and J. Hafner, Phys. Rev. B **58**, 5378 (1998).
[11] G. Trambly de Laissardière and T. Fujiwara, Phys. Rev. B **50**, 9843 (1994).
[12] A. Smontara, I. Smiljanić, J. Ivkov, D. Stanić, O. S. Barišić, Z. Jagličić, P. Gille, M. Komelj, P. Jeglič, M. Bobnar, and J. Dolinšek, Phys. Rev. B **78**, 104204 (2008).
[13] M. Komelj, J. Ivkov, A. Smontara, P. Gille, P. Jeglič, and J. Dolinšek, Solid State Commun. **149**, 515 (2009).
[14] J. Dolinšek, M. Komelj, P. Jeglič, S. Vrtnik, D. Stanić, P. Popčević, J. Ivkov, A. Smontara, Z. Jagličić, P. Gille, and Yu. Grin, Phys. Rev. B **79**, 184201 (2009).
[15] J. Dolinšek, P. Jeglič, M. Komelj, S. Vrtnik, A. Smontara, I. Smiljanić, A. Bilušić, J. Ivkov, D. Stanić, E. S. Zijlstra, B. Bauer, and P. Gille, Phys. Rev. B **76**, 174207 (2007).
[16] J. Dolinšek, S. Vrtnik, A. Smontara, M. Jagodič, Z. Jagličić, B. Bauer, and P. Gille, Philos. Mag. **88**, 2145 (2008).
[17] D. W. Deng, Z. M. Mo, and K. H. Kuo, J. Phys.: Condens. Matter **16**, 2283 (2004).
[18] J. Grin, U. Burkhardt, M. Ellner, and K. Peters, Z. Kristallogr. **209**, 479 (1994).
[19] J. Grin, U. Burkhardt, M. Ellner, and K. Peters, J. Alloys Compd. **206**, 243 (1994).
[20] R. C. Hudd and W. H. Taylor, Acta Crystallogr. **15**, 441 (1962).
[21] B. Zhang, V. Gramlich, and W. Steurer, Z. Kristallogr. **210**, 498 (1995).
[22] L.-E. Edshammar, Acta Chem. Scand. (1947-1973) **18**, 2294 (1964).
[23] L.-E. Edshammar, Acta Chem. Scand. (1947-1973) **19**, 2124 (1965).
[24] Z. A. Chaudhury and C. Suryanarayana, J. Less-Common Met. **91**, 181 (1983).
[25] P. Gille and B. Bauer, Cryst. Res. Technol. **43**, 1161 (2008).
[26] L. Zhang, Y. Du, H. Xu, C. Tang, H. Chen, and W. Zhang, J. Alloys Compd. **454**, 129 (2008).
[27] M. Döblinger, R. Wittmann, and B. Grushko, J. Alloys Compd. **360**, 162 (2003).
[28] L. G. Akselrud, P. Y. Zavalii, Yu. Grin, V. Pecharsky, B. Baumgartner, and E. Wölfel, Mater. Sci. Forum **133-136**, 335 (1993).
[29] P. W. Selwood, *Magnetochemistry* (Interscience, New York, 1956), p. 78.
[30] Y. Yamada, Y. Yokoyama, K. Matono, and K. Fukaura, Jpn. J. Appl. Phys. **38**, 52 (1999).
[31] J. T. Markert, J. L. Cobb, W. D. Bruton, A. K. Bhatnagar, D. G. Naugle, and A. R. Kortan, J. Appl. Phys. **76**, 6110 (1994).
[32] U. Mizutani, *Introduction to the Electron Theory of Metals* (Cambridge University Press, Cambridge, 2001), p. 43.
[33] Shuyuan Lin, Guohong Li, and Dianlin Zhang, Phys. Rev. Lett. **77**, 1222 (1996).
[34] A. B. Kaiser, Phys. Rev. B **29**, 7088 (1984).
[35] U. Mizutani, *Introduction to the Electron Theory of Metals* (Ref. 32), p. 299.
[36] X. Gonze *et al.*, Comput. Mater. Sci. **25**, 478 (2002) the ABINIT computer program is a common project of the Université Catholique de Louvain, Corning Incorporated, and other contributors.
[37] J. P. Perdew and Y. Wang, Phys. Rev. B **45**, 13244 (1992).
[38] M. Fuchs and M. Scheffler, Comput. Phys. Commun. **119**, 67 (1999).
[39] N. Troullier and J. L. Martins, Phys. Rev. B **43**, 1993 (1991).
[40] A. Kokalj, Comput. Mater. Sci. **28**, 155 (2003); code available from http://www. xcrysden.org
[41] G. K. H. Madsen and J. Singh, Comput. Phys. Commun. **175**, 67 (2006).
[42] P. Volkov and S. J. Poon, Phys. Rev. B **52**, 12685 (1995).